Science Bulletin 64 (2019) 293–300

Contents lists available at ScienceDirect

Science Bulletin

journal homepage: www.elsevier.com/locate/scib

Science Bulletin
www.scibull.com

Article

A family of high-temperature ferromagnetic monolayers with locked spin-dichroism-mobility anisotropy: MnNX and CrCX (X = Cl, Br, I; C = S, Se, Te)

Cong Wang [1], Xieyu Zhou [1], Linwei Zhou, Ning-Hua Tong, Zhong-Yi Lu, Wei Ji *

Beijing Key Laboratory of Optoelectronic Functional Materials & Micro-Nano Devices, Department of Physics, Renmin University of China, Beijing 100872, China

ARTICLE INFO

Article history:
Received 27 November 2018
Received in revised form 18 January 2019
Accepted 15 February 2019
Available online 20 February 2019

Keywords:
Two-dimentional materials
First-principles calculation
Strong mobility anisotropy
Spin-locked linear dichroism
High-temperature ferromagnets
Direct bandgap semiconductor

ABSTRACT

Two-dimensional magnets have received increasing attention since $Cr_2Ge_2Te_6$ and CrI_3 were experimentally exfoliated and measured in 2017. Although layered ferromagnetic metals were demonstrated at room temperature, a layered ferromagnetic semiconductor with high Curie temperature (T_c) is yet to be unveiled. Here, we theoretically predicted a family of high T_c ferromagnetic monolayers, namely MnNX and CrCX (X = Cl, Br and I; C = S, Se and Te). Their T_c values were predicted from over 100 K to near 500 K with Monte Carlo simulations using an anisotropic Heisenberg model. Eight members among them show semiconducting bandgaps varying from roughly 0.23 to 1.85 eV. These semiconducting monolayers also show extremely large anisotropy, i.e. $\sim 10^1$ for effective masses and $\sim 10^2$ for carrier mobilities, along the two in-plane lattice directions of these layers. Additional orbital anisotropy leads to a spin-locked linear dichroism, in different from previously known circular and linear dichroisms in layered materials. Together with the mobility anisotropy, it offers a spin-, dichroism- and mobility-anisotropy locking. These results manifest the potential of this 2D family for both fundamental research and high performance spin-dependent electronic and optoelectronic devices.

1. Introduction

In the past decades, a plenty of methods, e.g. magnetic or non-magnetic dopants [1–7], vacancies [8,9] and grain boundaries [10,11], have been attempted to introduce long-range ferromagnetic orders in semiconductors. The long range order is, however, limited by the dopant-host hybridization [2,12] that the highest T_c was thus recorded at ~200 K [4,13–15] in Mn-doped semiconductors and the mobility remains low. A T_c of 340 K was observed in a new class of heavily Fe-doped materials [6,16], which show metallic behaviors rather than semiconducting characteristics. It thus calls additional strategies for searching high T_c ferromagnetic semiconductors. Recently, the re-discovery of mono- or few-layer two-dimensional (2D) materials, e.g. borophene [17], MoS_2 [18–20] and black phosphorus (BP) [21–23] boosted tremendous investigations on 2D semiconductors and their heterostructures [24–26]. Two intrinsic ferromagnetic semiconducting mono (bi)-layers, i.e. CrI_3 [27,28] and $Cr_2Ge_2Te_6$ [29–31], were very recently demonstrated in experiments, although their Curie temperatures (T_c) are lower than 50 K. Thus, the high-T_c ferromagnetic (FM) semiconductors are yet to be discovered although room-temperature FM metallic monolayers, e.g. VSe_2 [32,33] and Fe_3GeTe_2 [34–36], were experimentally prepared or exfoliated, although with limited air-stability.

The lack of interlayer magnetic interactions at the monolayer limit enables a variety of interlayer antiferromagnetic (AFM) or weakly FM coupled materials to be under consideration for FM semiconductors, in which the constraint of strong FM interlayer coupling was eliminated. The CrI_3 mono- and bi-layers are exactly the case that they show an in-plane FM order and a weak interlayer AFM coupling below 50 K [28]. In a recent work, we found a strong electron doping (~1 *e*/Cr) to CrS_2 could lead this AFM metal to a FM semiconductor [37]. This doping could be realized by substituting Cr with Mn. Monolayer MnS_2 or $MnSe_2$ was predicted to be a FM semiconductor with a T_c of ~200 K [38]. A $MnSe_2$ monolayer, with a measured room-temperature T_c, was recently fabricated by molecular beam epitaxy (MBE) although the monolayer strongly interacts with the substrate and is yet to be exfoliated [39]. Another route to realize the doping lies in replacing an S atom with a Cl atom forming a monolayer CrSCl. A Janus CrSCl monolayer is a FM semiconductor that is 85 meV/Cr more stable compared with other magnetic configurations [37], suggesting it to be a promising candidate for high-T_c magnetic semiconductors.

Here, we theoretically predicted another structural form of CrSCl (Fig. 1a) and its analogues, e.g. CrCX and MnNX (C = S, Se, Te and X = Cl, Br, I). This form is energetically more stable than

* Corresponding author.
E-mail address: wji@ruc.edu.cn (W. Ji).
[1] These authors contributed equally to this work.

https://doi.org/10.1016/j.scib.2019.02.011
2095-9273/

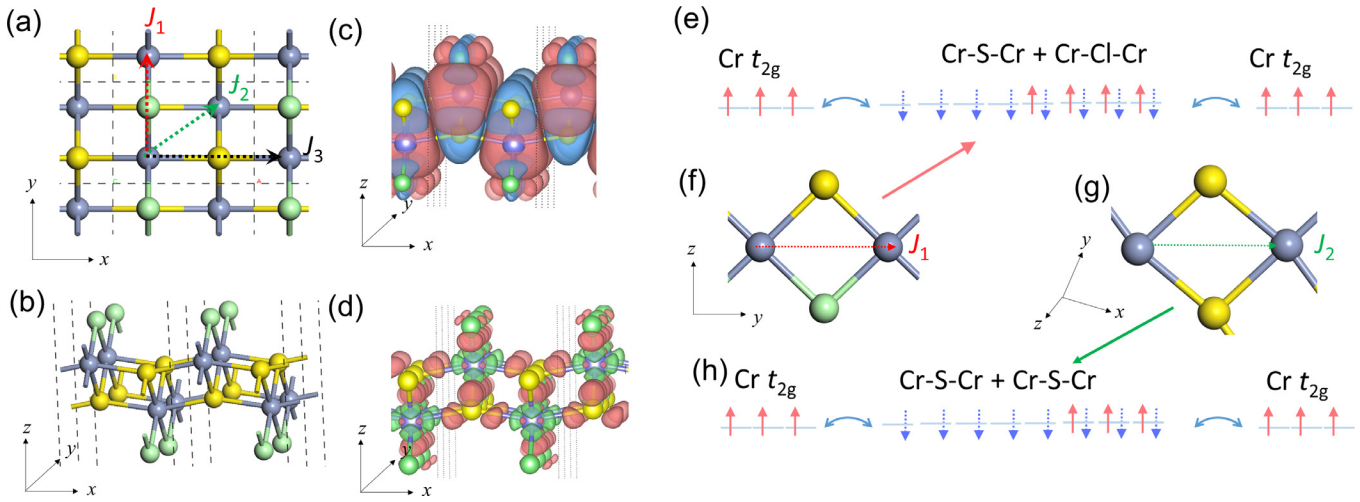

Fig. 1. Magnetic mechanism of CrCXs monolayers. (a), (b) Top and perspective views of a CrSCl monolayer in the orthogonal structure. Slate-blue, yellow and light green balls represent Cr, S and Cl atoms, respectively. The intralayer SEC parameters J_1, J_2, J_3 between Cr sites are represented with dashed arrows. (c) Perspective view of the spin charge density of CrSCl in the FM order plotted with an isosurface value of 0.001 e/Bohr^3. Red and blue isosurface contours correspond to charges polarized in up and down spins, respectively. (d) Perspective view of the atomic differential charge density of the CrSCl monolayer plotted with an isosurface value of 0.01 e/Bohr^3. Red and green isosurfaces correspond to the charge accumulation and reduction after Cr, S and Cl atoms bonding together, respectively. (e) Schematic of the FM double-exchange mechanism for spin-exchange through a Cr-S-Cr and a Cr-Cl-Cr channels (denoted J_1) as illustrated in (f), in which red up-oriented and blue down-oriented arrows represent electrons with different spins. By following the same scheme, panels (g) and (h) show the atomic structure and spin-exchange coupling mechanism of the two Cr-S-Cr channels (denoted J_2), respectively.

the Janus monolayers and does not have inherently existed unbalanced in-plane strain. This form, different from the hexagonal Janus [37], CrI_3 [28], $RuCl_3$ [40] $Cr_2Ge_2Te_6$ [29] and Fe_3GeTe_2 [34] monolayers, has two nearest and four second-nearest neighbors, twice the number of previous candidates in hexagonal lattices. Curie temperatures of these monolayers were predicted using Monte Carlo simulations with a third-nearest anisotropic Heisenberg (AH) model. The maximum T_c values are over 240 K and near 500 K for semiconducting and metallic monolayers, respectively, which are much more superior to CrOCl [41], a lighter member of CrCXs with our predicted T_c of 16 K. The bandgaps of these materials are primarily determined by the chalcogen atom, varying from nearly 2 to 0 eV, while eight of them are FM semiconductors and another four of them are FM metals with T_c up to 492 K. In addition, this MnNX and CrCX family does not show strong structural anisotropy, but the electronic structures, carrier mobility and their resulting optical absorption are highly anisotropic and are locked together. All these results may boost experimental studies on this novel family of 2D magnetic monolayers with extraordinarily high T_c values.

2. Methods

2.1. DFT calculations

Our density functional theory (DFT) calculations were performed using the generalized gradient approximation for the exchange-correlation potential, the projector augmented wave method [42,43] and a plane-wave basis set as implemented in the Vienna ab-initio simulation package (VASP) [44,45] and Quantum Espresso (QE) [46]. Dispersion correction was made at the van der Waals density functional (vdW-DF) level [47–49], with the optB86b functional for the exchange potential, which was proved to be accurate in describing the structural properties of layered materials [23,50–54] and was adopted for structure related calculations. For energy comparisons among different magnetic configurations, we used either the PBE [55] or hybrid (HSE06) functional [56,57], with the inclusion of spin–orbit coupling (SOC), based on the vdW-DF revealed structures. Density functional perturbation theory [58] was employed to calculate phonon dispersion (QE) and vibrational frequencies at the Gamma point (VASP). In VASP calculations, the kinetic energy cut-off for the plane-wave basis set was set to 700 eV for geometric and 400 eV for electronic structures calculations by the HSE06 functional. A k-mesh of $10 \times 14 \times 1$ was adopted to sample the first Brillouin zone of the conventional unit cell of monolayer CrCXs and MnNXs. The phonon dispersion was obtained by Fourier interpolation of the dynamical matrices calculated using an $18 \times 20 \times 1$ k-mesh and a $6 \times 4 \times 1$ q-mesh with a plane-wave energy cutoff of 50 Ry. On-site Coulomb interactions to the Cr d and Mn d orbitals are considered with U and J values ranging from 3.89 – 4.40 eV and 0.80 – 1.25 eV, respectively, as revealed by a linear response method [59] and listed in the Supplementary Table S1. These values are comparable to the values adopted in modeling CrI_3 [60,61] and CrS_2 [37]. The HSE06 functional already considers the exact exchange energy, the U and J correction does not apply to HSE06 calculations. The influences of different functionals and U, J values were also discussed in the Supplementary Figs. S1, S2. More calculation details were provided in the Supplementary Materials.

2.2. Curie temperature prediction

Spin-exchange coupling (SEC) parameters were extracted based on a third-nearest Heisenberg model,

$$H = H_0 + J_1 \sum_{\langle ij \rangle} S_i \cdot S_j + J_2 \sum_{\langle\langle ij \rangle\rangle} S_i \cdot S_j + J_3 \sum_{\langle\langle\langle ij \rangle\rangle\rangle} S_i \cdot S_j.$$

Here, J_1, J_2 and J_3 represent the first-, second- and third- nearest couplings, respectively, as illustrated in Fig. 1a. We derived the spin exchange parameters by the total energy differences of the four magnetic configurations shown in the Supplementary Fig. S3. The magnetic energy contributions of these magnetic configurations in each magnetic unit cell write as

$$E_{FM} = \frac{N^2}{4} \times \frac{1}{2}(2J_1 + 4J_2 + 2J_3),$$

$$E_{AFM1} = \frac{N^2}{4} \times \frac{1}{2}(2J_1 - 4J_2 + 2J_3),$$

$$E_{AFM2} = \frac{N^2}{4} \times \frac{1}{2}(2J_1 - 2J_3),$$

$$E_{AFM3} = \frac{N^2}{4} \times \frac{1}{2}(-2J_1 + 2J_3),$$

where N represents the unpaired spins on each Cr atom, which is chosen as 3 in our calculations.

Metropolis Monte Carlo simulations were carried out to predict Curie temperatures. A J_1-J_2-J_3 model was used to do the Metropolis Monte Carlo simulations, in which two nearest, and two next-next-nearest Cr (Mn) atoms were considered. This model is more advanced than the one only contains four next-nearest sites in a square lattice, as used in a previous work [41]. A 50×50 lattice was used for all simulations and each lattice point include 2 Cr (Mn) atoms. Simulation results revealed with the Ising model show high T_c values from 271 to 1,179 K. However, the anisotropy was largely overestimated in the Ising model, which leads to the predicted T_c values two or three times the exact values. We eventually used an anisotropic Heisenberg model in order to make the simulation results more sensible in comparison with experiments.

$$H = -\left(\frac{J}{2}\sum_{i,i'} \boldsymbol{S_i} \cdot \boldsymbol{S_{i'}} + \sum_i D_e\left(S_i^e\right)^2 + \frac{\lambda_e}{2}\sum_{i,i'} S_i^e \cdot S_{i'}^e\right).$$

The first term in the Hamiltonian describes the isotropic exchange while the final term is the anisotropic symmetric exchange between different sites. The term with D represents the easy axis single-ion anisotropy. Instead of the continuous flipping in the Heisenberg model, we fix the spin-flipping in only six directions: (1,0,0), (−1,0,0), (0,1,0), (0,−1,0), (0,0,1), (0,0,−1); this simplification greatly speeds up simulation processes with a reasonable error of less than 10% as double checked in the Supplementary Fig. S4d. A hexagonal lattice was used for simulating the CrI_3 monolayer, which yields a T_c value of 65 K, very close to the analytical solution of 63 K; this verifies the reliably of the model. A T_c value of 43 K was found through the anisotropic Heisenberg model, which is exceedingly closed to the experimental value of 45 K. In addition to MC simulations, we also employed renormalized spin wave theory (RSWT) to predict T_c values. The details of the derivation and the numerical results of our RSWT calculations were provided in the Supplementay materials (Supporting Information II).

2.3. Carrier mobility estimation

Phonon-limited carrier mobility in CrSeBr monolayers with a finite thickness W_{eff} is expressed as [51,62,63]:

$$\mu_{film} = \frac{\pi e\hbar^4 C_{film}}{\sqrt{2}(k_B T)^{3/2}(m^*)^{5/2}\left(E_1^i\right)^2} F.$$

Here, m^* represents the effective mass along the transport direction and E_1 is the deformation potential constant of the VBM (hole) or CBM (electron) along the transport direction, which is determined by $E_1^i = \Delta V_i/(\Delta l/l_0)$. Here ΔV_i is the energy change of the i^{th} band under proper cell compression and dilatation (by a step 0.5%), l_0 is the corresponding lattice constant along the transport direction and Δl is the deformation of lattice constant. Variable C_{film} is the elastic modulus of the longitudinal strain in the propagation direction, which is derived by $(E - E_0)/V_0 = C(\Delta l/l_0)^2/2$; E represents the total energy and V_0 represents the lattice volume at the equilibrium for 2D systems. A crossover function F bridges the 2D and 3D cases, which is estimated by

$$F \equiv \frac{\sum_n \left\{\frac{\sqrt{\pi}}{2}[1 - \mathrm{erf}(\Omega(n))] + \Omega(n)e^{-\Omega^2(n)}\right\}}{\sum_n [1 + \Omega^2(n)]e^{-\Omega^2(n)}},$$

where

$$\Omega(n) \equiv \sqrt{\frac{n^2\pi^2\hbar^2}{2m^* W_{eff}{}^2 k_B T}}.$$

The erf() represents an error function and the summation over integer is due to quantum confinement along the z-direction. Effective thickness of the film (W_{eff}) is expressed by

$$\frac{1}{W_{eff}} = \int_{-\infty}^{+\infty} P_i(z)P_f(z)dz = \sum_n \frac{\rho_i^n(z)}{N\Delta z} \cdot \frac{\rho_f^n(z)}{N\Delta z}\Delta z.$$

Here, $P(x)$ is the electron probability density along the z direction. We divided the space along the x direction into n parts by Δz. Variable $\rho^n(z)$ is the sum of the number of electrons n^{th} region along the z direction. Here, N is the total number of valence electrons in the film, i and f represent equilibrium and deformed films, respectively. The electronic structures in carrier mobility elimination are all calculated with the HSE06 functional. We implemented these carrier mobility estimation methods in a computer package, "Renmin Mobility Calculator" (ReMoC). Please visit http://sim.phys.ruc.edu.cn/tools/ for details.

2.4. Optical absorption spectra and conductivity calculation

The absorption spectra were calculated from the dielectric function using expression [23,51] $A(\omega) = \alpha(\omega)\cdot\Delta z$, where $\alpha(\omega) = \frac{\omega \mathrm{Im}\varepsilon}{cn}$ is the absorption coefficient, $n = \sqrt{\frac{\sqrt{(\mathrm{Re}\varepsilon)^2 + (\mathrm{Im}\varepsilon)^2} + \mathrm{Re}\varepsilon}{2}}$ is the index of refraction, $\mathrm{Re}\varepsilon$ and $\mathrm{Im}\varepsilon$ are the real and imaginary parts of the dielectric function [64], respectively. ω is the light frequency, c is the speed of light in vacuum and Δz represents the unit-cell size in the z direction. The conductivity tensor was calculated from the imaginary parts of the dielectric function as well, $\sigma_{ij} = \frac{\omega}{4\pi}\mathrm{Im}\varepsilon_{ij}$, where i, j represent the directions x, y and z. The electronic structures were obtained from the results unveiled using the PBE functional and the k-mesh was increased to $28 \times 32 \times 1$ in calculating dielectric functions. Enough conduction bands were considered and exciton effects were not considered in the optical properties calculations. Because the dielectric function is a tensor, the absorption spectra along the x, y and z directions were obtained separately. The energies of incident light of the horizontal axis in absorption spectra were shifted by the differences of bandgaps between the PBE + U-J (-SOC) and HSE06 (-SOC) results.

3. Results and discussion

Figs. 1a and 1b show a top- and a perspective-views of the fully relaxed atomic structure of CrSCl in the CrCXs form while its other less stable forms, e.g. 1T-Janus, are available in the Supplementary Fig. S5 and Table S2. Phonon dispersion spectra are also available in the Supplementary Fig. S6 indicating the stability of the CrCXs form. We used CrSCl as an example that it is comprised of perpendicularly oriented Cr-S/Cl rhomboid chains along y and distorted Cr-S rectangular chains along x. The shortest Cr-Cr distance of 3.44 Å was found in the rhomboid chains, being bridged by an S and a Cl atoms. We denote the SEC parameter of this interaction as J_1 (red arrow). The second-nearest Cr-Cr interaction is bridged by two S atoms with a distance of 3.61 Å and a Cr-S-Cr angle of 91.5°, the SEC parameter of which is denoted as J_2 (green arrow). In addition, SEC parameter J_3 represents a nearly linear Cr-S-Cr

interaction (black arrow). Detailed structural information of CrCXs and MnNXs can be found in the Supplementary Table S3. The derivation details of these three parameters are available in the Section 2.

The FM state in all CrCXs and MnNXs is energetically more stable than other magnetic configurations regardless which functional is used and whether U or/and J is/are added, as shown in the Supplementary Fig. S3. By comparing their total energies, we derived J_1 = 0.90 meV, J_2 = 2.98 meV and J_3 = 1.26 meV for CrSCl. Exact SEC parameters and predicted Curie temperatures are listed in Table 1. Here, we used a classical magnetic moment S = 3/2 according to the DFT value of roughly 3 μ_B per Cr atom. Although J_2 represents a 0.17 Å longer distance than J_1, the coupling strength of J_2 is triple that of J_1. Replacement of Cl with Br or I substantially enlarges J_1 and slightly enlarges J_2 and J_3 in the S/Se-series, leading to nearly comparable J_1 and J_2 for the I-series monolayers. The Te-series is fairly different from the S/Se-series that the comparable J_1 and J_2 values increase from Cl to I and J_3 drops from nearly 16 meV to a small negative value (−1.9 meV), leading to small J_1 and J_2 and pronounced J_3 in CrTeCl and three times larger J_1 and J_2 and negative J_3 in CrTeI. All these three parameters gradually enlarge from Cl to I in the MnN-series and those of MnNI are significantly large.

Either spin density (Fig. 1c) or atomic differential charge density (aDCD, Fig. 1d) shows the origin of magnetism from the Cr t_{2g} orbitals where three Cr 3d electrons fill in. The aDCD indicates charge reduction on Cr e_g orbitals forming sigma bonds with chalcogen or halogen 3p orbitals. The spin density indicates the spin-up (red) was primarily originated from Cr t_{2g} orbitals and partially from halogen p_z orbitals. The spin-down (blue) components are mainly contributed by all three chalcogen p and partially by both halogen p_x and p_y orbitals, suggesting the super-exchange FM coupling along the J_1 or J_2 direction bridged by S or Cl atoms.

Fig. 1e–h summarize a diagram of the orbital filling and their magnetic interactions, which were compellingly supported by the orbital-decomposed bandstructures (the Supplementary Fig. S7). In particular, two Cr atoms are bridged by a Cl and an S atom for the J_1 interaction (along the y direction), which involves two of six sp^3d^2 hybridized orbitals for each Cr and two orthogonal $p_{x/y}$ orbitals for each Cl or S, totally eight orbitals. In a valence band picture, each Cr orbital is originally filled by 3/2 electrons while 5/3 and 4/3 electrons for each Cl and S orbitals, respectively. These eight orbitals are thus filled by 6e from Cr, 10/3 e from Cl and 8/3 e from S, totally 12e. Therefore, four states are only filled by spin-down electrons (Figs. 1e and f), which is consistent with the spin density plotted in Fig. 1d. These orbitals offer four channels of virtual hopping for the spin up electrons of the Cr t_{2g} orbitals; this strongly favors FM coupling and is consistent with the Hund's rule. This picture also explains the always slightly stronger J_2 than J_1 that the Cr-S-Cr coupling (Fig. 1g and h), having a 2/3 e reduced number of filling electrons, offers an additional partial channel for FM coupling to the Cr-Cl-Cr coupling. It also suggests that a reduced number of the filling spin-down electrons of the bridging atoms may open more hopping channels and thus enlarge the value of T_c, which was elucidated by the 492 K T_c of the MnNI monolayer (see Table 1).

In a local moment picture, the linear Cr-S-Cr coupling (J_3) usually favors AFM. Here, the hybridization of chalcogen p_z with Cr d_{z^2} orbitals form delocalized bonding and antibonding states (see Fig. 2 and Supplementary Fig. S8). The bonding state is occupied and itinerant electrons of this state dominate and mediate a FM coupling between two adjacent Cr cations, which is reinforced by kinetic energy gains [65]. Therefore, the linear J_3 gives rise to FM coupling in the CrS/Se- and MnN-series. In the Te-series, the Cr d_{z^2} orbitals become partially occupied and dominate the bandstructures around the Fermi level thus leading to a strong itinerant FM in the monolayer limit; this explains the fairly large FM J_3 in CrTeCl. The occupation of the antibonding conduction bands gradually reduces from CrTeCl to CrTeI (the Supplementary Figs. S9g–S9i). Therefore, the super-exchange AFM coupling is eventually overcome the FM coupling, leading to a small AFM J_3 for CrTeI.

Monte Carlo simulations were performed with an anisotropic Heisenberg (AH) model and a three-nearest Ising model (see the Supplementary Fig. S4 and Methods for details). Here, the AH model considers both on-site and spin-spin anisotropies, which play a key role when the thickness of a layered materials reduces to its 2D limit. The on-site anisotropy is primarily a result of spin–orbit coupling (SOC). For spin-spin interactions, we used a simplified model where the interactions along two hard magnetization axes were averaged. Table 1 shows the single-ion magnetic anisotropy energies (MAEs) of all considered CrCXs/MnNXs. The easy axes of CrSCl, CrTeBr, CrTeI, MnNCl and MnNBr were found parallel to the z direction. This group contains direct and indirect bandgap semiconductor and metals with both highly dispersive and nearly flat bands around the Fermi Level. Table 1 also shows the RSWT predicted T_c values. The RSWT simulations give nearly identical T_c values to the MC results for CrSBr and CrSeI. For other layers, The RSWT results show substantially higher T_c values compared with MC calculations, except for CrTeI where RSWT predicts a value of 86 K while MC gives a value of 139 K. We found the use of HSE leads to larger FM spin-exchange parameters and reinforced

Table 1
Magnetic properties of the 12 monolayers, including the intralayer spin-exchange coupling parameters J_1, J_2, J_3, anisotropic spin-spin exchange parameter λ and easy axis single ion anisotropy D, easy axis direction, Curie temperatures predicted using Ising model, anisotropic Heisenberg (AH) model and RSWT, bandgaps without on site Coulomb U and exchange J (w/o UJ), bandgaps with and without spin-orbit coupling revealed with the HSE06 functional and PBE + U-J.

Magnetic monolayers	Exchange parameters (meV/Cr)					Easy axis	T_c (K)			Bandgap (eV)	
	J_1	J_2	J_3	λ	D		Ising	AH	RSWT	HSE/-SOC	PBE + U-J/ -SOC
CrSCl	0.90	2.98	1.26	0.01	−0.02	z	271	108	320	1.86/1.85	1.40/1.52
CrSBr	1.66	3.09	1.52	-2×10^{-3}	0.02	x	313	127	124	1.76/1.68	1.36/1.45
CrSI	2.49	3.07	1.69	-4×10^{-4}	0.06	y	352	146	181	1.21/1.09	0.89/1.01
CrSeCl	1.32	3.40	0.56	0.02	−0.01	y	284	118	213	0.85/0.81	0.57/0.86
CrSeBr	2.09	3.52	0.76	0.01	-4×10^{-3}	y	326	135	227	0.96/0.89	0.64/0.87
CrSeI	3.12	3.67	1.18	-1×10^{-3}	0.02	y	391	164	164	0.74/0.55	0.46/0.62
CrTeCl	1.45	1.42	16.28	0.05	0.15	x	589	248	377	−*/−*	−*/−*
CrTeBr	2.91	2.68	4.61	0.48	−0.75	z	448	187	582	−*/−*	−*/−*
CrTeI	4.56	4.13	−1.90	−0.10	0.55	z	304	139	86	−*/−*	−*/−*
MnNCl	5.53	4.15	3.35	0.02	0.07	z	600	238	376	0.44/0.68	0.47/0.46
MnNBr	5.66	3.68	5.41	0.03	0.02	z	652	261	469	−*/0.23	0.32/0.33
MnNI	14.14	5.71	8.19	−0.03	0.93	x	1179	492	741	−*/−*	−*/−*
CrI_3	1.62	N/A	N/A	0.08	0.06	z	65	43	52	N/A	N/A
CrOCl	−0.02	0.07	1.46	-2×10^{-3}	0.02	z	29	16	12	3.20/	2.47/2.54

* Stands for metal.

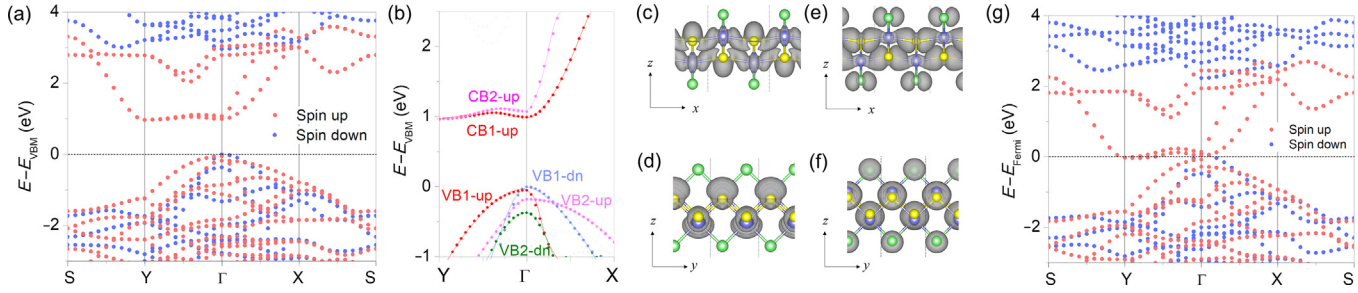

Fig. 2. Electronic structures of CrSeBr. Spin-resolved, i.e. red for spin-up and blue for spin-down, electronic band structure of CrSeBr were calculated with the HSE06 functional (a). A simplified bandstructure of CrSeBr around the G point was plotted in (b). Wavefunction norms of spin-up CB2 along G-X and G-Y were shown in (c) and (d), respectively, while those for spin-up VB1 were depicted in (e) and (f). The isosurface value was set to 0.001 e/Bohr^3. Spin-resolved electronic band structure of CrTeI calculated with the HSE06 functional was shown in (g).

spin–spin and on-site FM couplings for magnetic anisotropy (the Supplementary Table S4); this thus results in higher transition temperatures. In light of this, our predicted transition temperatures using MC are rather conservative and the measured T_c values might be even larger than our predicted values.

In terms of metallic layers, MnNI has the highest T_c of 492 K and the lowest one of 139 K was found in CrTeBr. The bandgap of MnNBr is less conclusive that the HSE and PBE + U-J calculations suggest different results. These metallic FM monolayers, serving as FM metals in transitional magnetic devices, offer flexibility and largely reduced thickness in 2D magnetic devices. The T_c values of semiconducting monolayers were lower than those of metallic layers. In particular, the highest T_c of 238 K (600 K with the Ising Model and 376 K with RSWT) was found in MnNCl (Table 1) with the easy axis along z while the lowest T_c is 108 K for CrSCl (AH model value) or 124 K for CrSBr (RSWT value). These values are roughly five times and twice the measured value of 45 K [28] and this-work predicted value of 43 K for CrI_3. Here, a T_c over 200 K approaches the room temperature and is subject to further substrate induced enhancement, as found in the $MnSe_2$ [38,39] and $Cr_2Ge_2Te_6$ [29] cases, and the doping enhancement as realized in Fe_3GeTe_2 [34–36].

Table 1 suggests that the S- and Se-series, MnNCl and MnNBr (inconclusive) are semiconductors with varying bandgaps from 1.85 to 0.23 eV (HSE-SOC)/1.52 to 0.33 (PBE + U-J-SOC), among which CrSeCl is of a near direct-bandgap (direct- and indirect-bandgaps differ by 0.5 meV) and CrSCl also offers a small difference of 6 meV. According to a private communication with Yu Ye from Peking University, PBE + U-J-SOC result, with our linear-response derived U and J values, for the bandgap of CrOCl layers appears to be closer to the experimental value than that of HSE. In light of this, our U and J values should be very close to the set fitted using bandgaps. However, we cannot rule out the role of defects in the bandgap measurements, we thus used the HSE values in our following discussion on electronic and optical properties, which are independent from U and/or J values and were found comparable with experimental values in 2D layers. Fig. 2a depicts the bandstructure of CrSeBr because of its moderate bandgap (0.89 eV, in the infrared range), high predicted T_c and a representative bandstructure of CrCXs. Bandstructures of other monolayers calculated with different functionals were shown in the Supplementary Figs. S9–S12.

Strong anisotropy, nearly linear dispersion and a roughly flat band are more clearly shown in a simplified bandstructure of CrSeBr (Fig. 2b), which contains two spin-up CBs, two spin-up and two spin-down VBs, respectively. The spin-up CB2 (pink) is comprised of Cr d_{z^2} and Se/Br p_z orbitals (Supplementary Fig. S7b–d), which exceptionally form extended Cr-Se-Cr channel states along the x direction (Fig. 3c) but highly localized along the y direction (Fig. 3d), giving rise to a quasi-1D electronic state in a 2D orthogonal lattice. Note that we define the d_{z^2} or p_z direction along the x direction and p_x, p_y and $d_{x^2-y^2}$ along the Cr-X (X = Cl, Br and I) bonding directions (see Supplementary Fig. S7a). This quasi-1D state offers a small effective mass of 0.06 m_0 along G-X but a rather large effective mass of 1.18 m_0 along G-Y, leading to the mobility (6.10×10^3 cm^2/V s) for spin-up CB2 along x 68 times that along y (0.09×10^3 cm^2/V s) (Supplementary Table S5). State spin-up CB1 (red) shares the same feature but its wavefunction is more localized along either x or y (Supplementary Fig. S8f and 8h), consistent with the larger effective masses of $0.40m_0$ and $7.1m_0$, respectively. The position of the spin-down component of CB sites over 1 eV higher than the spin-up CBM, while it also slightly depends on U values in PBE + U-J calculations (see the Supplementary Fig. S1).

Spin-up VBs are rather interesting that the anisotropy of effective masses was found in either spin-up-VB1 (red) and -VB2 (pink), both of which are composed of Se/Br p_z and Cr d_{z^2} orbitals (Supplementary Fig. S7e-g). The spin-up-VB1 appears a nearly mirror analogue to that of spin-up-CB1 with respect to the gap around the G point, namely $m_x = 0.06\ m_0$ and $m_y = 1.30\ m_0$ (Supplementary Table S5), which shares the same mechanism of the CB case (Fig. 2e and f). The mass anisotropy of spin-up-VB2, i.e. $0.53m_0$ (y) and $2.66\ m_0$ (x), is reversal to spin-up-VB1 along the x and y directions. A similar behavior was found for those two spin-down VBs (blue and green) with less pronounced anisotropy (Supplementary Fig. S8 and Table S5). In CrSeBr, spin-down-VB1 serves as the highest VB, which may change in other CrCXs, e.g. in CrSCl, where the monolayer becomes a nearly direct-bandgap half-semiconductor (Fig. 3 and Supplementary Fig. S9).

The giant effective masses found along either direction for these bands imply likely strong correlation of VBs or doped CBs, which is, most likely, more pronounced in CrTeI (Fig. 2g). It shows a nearly flat-band along G-Y near E_F, which is even flatter and closer to E_F with the inclusion of SOC (Supplementary Fig. S10i). Such a flat band mixed with two spin components might suggest emerging physical phenomena with strong correlation. In terms of MnNXs, they contain band crossings along G-Y with likely band inversions. The semiconducting MnNCl is a result of interaction induced gap-opening (Supplementary Fig. S10e). Other semiconducting layers, except MnNCl, show similar anisotropic features and share the same mechanism of anisotropy (Supplementary Fig. S9). This general spin-dependent mobility anisotropy suggests spin-up electron carriers moving much faster along the x direction than along the y direction and the reversal for hole carriers. If an off-axis in-plane electric field is established, spin accumulation might be observed in the more localized y direction, which may potentially be used in transferring spin torques. All band structures and detailed energy levels of VBM and CBM of CrCXs and MnNXs are available in Fig. 3 and Supplementary Fig. S9.

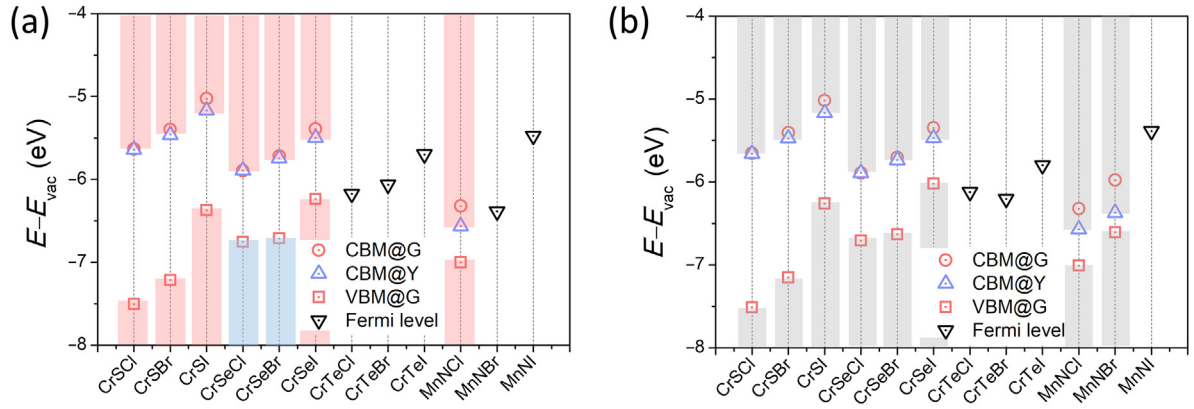

Fig. 3. Energy positions of CBM, VBM or the Fermi level of CrCX monolayers. The energy positions were obtained from the HSE06 (a) and HSE06-SOC (b) results, respectively. The vacuum level was set as the reference zero. Red and blue bars indicate the spin-up and -down components, respectively. In the MnNCl/MnNBr monolayer, the blue triangle shows the position of its CBM which sits at a point between G and Y. The Fermi levels in all metallic monolayers were labeled with black triangles.

Figs. 3a and b plot the positions of CBMs and VBMs calculated without and with SOC, respectively. The energy levels of CBM at G and Y have tiny differences below 0.15 eV and an 1% in-plane strain can induce a transition between indirect and direct bandgap. It is exceptional that the energy positions of the CBMs for all semiconducting CrCXs and MnNCl monolayers are rather deep, from −5.17 to −6.57 eV, suggesting the anisotropy of CBs could be feasibly utilized in practical devices. The band alignments indicate the possibility of constructing type-I (e.g. CrSeI/CrSI), type-II (e.g. CrSeCl/CrSeI) and type-III (e.g. CrSeI/MnNCl) heterostructures. The type-III heterostructures are of particular interest that they may be employed to build Dirac-source devices with the subthreshold swing smaller than 60 meV/decade [66].

Fig. 4a shows a sketch-map of the bands around the G point of the CrSeBr monolayer. The CB energies at G and Y are nearly degenerated. Since the halogen atoms strongly affect the interactions along the *y* direction, heavier halogen atoms lead to more extended wavefunctions and thus show stronger band dispersions; this gives rise to flatter CBs and large splitting of spin-up-CB1 and -CB2 in CrSCl than those in CrSI (Supplementary Figs. S9 and S11). An exchange-induced enhancement of CB splitting at G was found when comparing results using the hybrid HSE06 functional with those of PBE + U-J (Supplementary Figs. S9 and S11). In addition, the inclusion of spin-spin exchange *J* or on-site *U* term in HSE calculations, as a result of overestimated FM exchange, enlarges the splitting of the two CB at the G point (Supplementary Fig. S2), resulting in a lower energy of CB at G than Y, which, we believe, is an artefact in the groundstate but might be valid under certain external fields. These results highlight the importance of exchange interactions in obtaining direct bandgap at the G point in CrCXs.

The optical conductivity [67] (Fig. 4c) and the light absorbance [51,64] (Fig. 4d), explicitly show a spin-selective linear dichroism. In particular, only the up-spin component has absorbance in an energy range from 1.05 eV (transition from spin-up-VB1 to -CB1) to 2.27 eV while the down-spin component becomes excitable by light with even higher energies; this allows to generate pure spin-polarized photo-current using light linearly polarized in certain directions. In this range, light linearly polarized along the *x* direction has much higher absorbance (4.26% per layer at 2.00 eV) than that along the *y* direction (0.31% per layer at 2.00 eV), showing a spin-selective linear dichroism, in other words, a spin-dichroism locking. This spin-locked linear dichroism is thus substantially different common spin-dependent optical excitations by left- or right-hand circularly polarized light in magnetic semiconductors and the circular dichroism led by valley physics in transitional metal dichalcogenides (TMDs) [68–74], as well as the linear dichroism induced by wavefunction asymmetry [20].

Although the absorption of CrSeBr initializes in the infrared range, this energy range is tunable to lower or higher energy range by substituting S or Cl with Se, Br or I atoms since it is highly relevant with the bandgaps. In the presence of Se, Br and I atoms, strong SOC eliminates symmetry forbidden rules of different spin

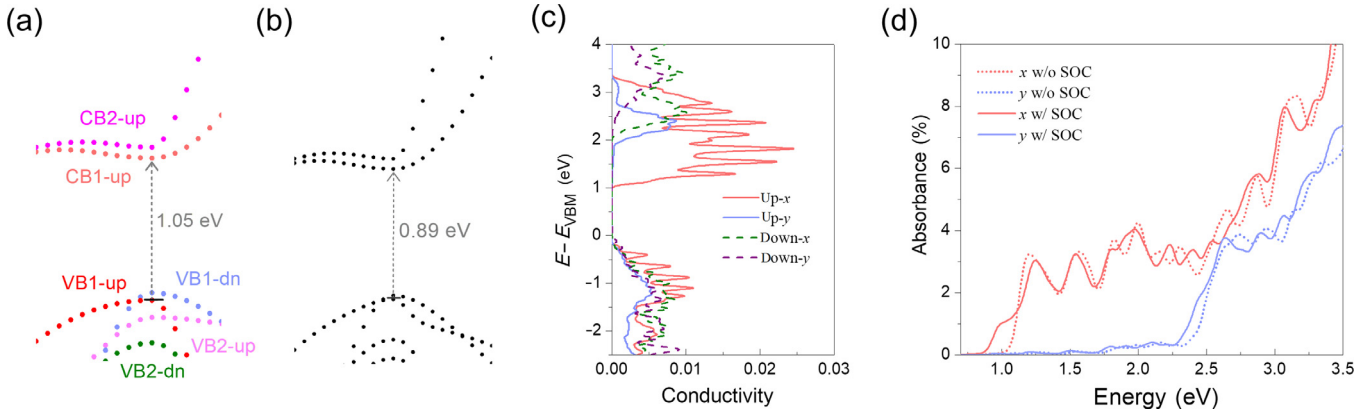

Fig. 4. Optical conductivity and absorbance. (a), (b) Sketch map of CB1, CB2, VB1 and VB2 of CrSeBr around the G point calculated with the HSE06 (a) and HSE06-SOC (b). (c) Spin resolved optical conductivities of different incident light polarization directions. (d) Absorbance of incident light polarized along the *x* (red) and the *y* (blue) directions in an energy range from 0.7 to 3.5 eV.

components, which shifts the absorption edge of CrSeBr from 1.05 to 0.89 eV (Fig. 4d) since the both spin channels could be excited to the CB states. Therefore, we infer CrSeI (with a gap of 0.55 eV, equivalently 2,255 nm) may have better absorbance among these CrCXs. In addition, this dichroism suggests CrCX monolayers may be used to construct spin-optical selectors. In particular, pure spin-up photo-electrons, moving much faster in the x direction, were excitable only by linearly polarized lights along the same direction while the excitations of spin down electrons are forbidden; this might shed light on generating pure spin-polarized photo-current by only linear polarized incident light.

4. Conclusion

In summary, we discovered a family of ferromagnetic semiconducting and metallic monolayers, namely CrCXs and MnNXs, which share the same structure. Their T_c values are predicted up to 492 K with strong intra-layer and weak inter-layer magnetic couplings. Both localized and itinerant electrons contribute to the formation of the FM ordering. The strengths of these two competing coupling mechanisms are tunable by element substitutions. A reduced number of filling electrons to the chalcogen and halogen atoms was found a key factor for stronger FM couplings, which enlightens a strategy for searching other high T_c FM monolayers. Given over 100 K T_c for CrSCl, it turns out the strong SOC is not paramount in obtaining high T_c in 2D layers [75] while spin-spin interaction or orbital anisotropy does offer magnetic anisotropy, which opens an avenue for searching magnetic monolayers. Additional high T_c indicators include greater local magnetic moment (usually three t_{2g} electrons) and larger neighboring numbers.

Strong anisotropy is a key characteristic of this monolayer family. The spin-up VBs and CBs of semiconducting CrCXs show highly anisotropic electron and hole effective masses and mobilities that the mass ratio is up to 22 and the mobility ratios are near 670 between the x and y directions. Strongly dispersive S/Se p_z and Cr d_{z^2} states along x and nearly flat-band Cr d_{z^2} states along y were exceptionally found in CrCXs, resulting in the coexistence of nearly free-electron and highly correlated states. Here, the chalcogen atoms do not include O since the O-Cr polarization is much stronger than those in other bonds leading to more localized states. In addition to the previously revealed purely circular and linear dichroisms found in MoS_2 [68,69], BP [23,76,77] and other 2D materials [70–74], we found a spin-selective (locked) linear dichroism in 2D CrCX layers, showing a spin-dichroism-mobility locking effect. Only the spin-up component could be excited with linearly polarized light along the x direction and the excited spin-up electrons moving much faster along the same direction. Note that the energy difference between interlayer FM and AFM configurations for each CrCX or MnNX is roughly 1 meV/Cr or 1meV/Mn (not shown here) and the bulk form of CrSBr was experimentally synthesized [78]. These facts suggest the feasibility of experimental investigations and manipulations of the CrCXs and MnNXs monolayers. All these results compellingly indicate that the CrCXs/MnNXs family is a novel interesting category of FM monolayers for either spintronics or optoelectronics, which is experimentally accessible and is of high potential in applications.

Conflict of interest

The authors declare that they have no conflict of interest.

Acknowledgments

This work was supported by the National Natural Science Foundation of China (11274380, 91433103, 11622437 and 61674171), the Fundamental Research Funds for the Central Universities of China and the Research Funds of Renmin University of China (16XNLQ01), the Strategic Priority Research Program of Chinese Academy of Sciences (XDB30000000). C.W was supported by the Outstanding Innovative Talents Cultivation Funded Programs 2017 of Renmin University of China. Calculations were performed at the Physics Laboratory of High-Performance Computing of Renmin University of China and Shanghai Supercomputer Center.

Author contributions

Wei Ji designed the research. Cong Wang performed the calculations of the geometry structures, electronic structures and magnetic coupling parameters. Xieyu Zhou performed Metropolis Monte Carlo simulations and the calculations of the optical properties. Linwei Zhou coded program "Renmin Mobility Calculator" (ReMoC) for carrier mobility calculations. Ning-Hua Tong carried out the renormalized spin wave theory (RSWT) study of two-dimensional anisotropic Heisenberg model (2DAHM) on square lattice and on honeycomb lattice. Cong Wang, Xieyu Zhou, Ning-Hua Tong, Zhong-Yi Lu and Wei Ji analyzed the results and wrote the manuscript. All authors commented on the manuscript.

Appendix A. Supplementary data

Supplementary data to this article can be found online at https://doi.org/10.1016/j.scib.2019.02.011.

References

[1] Furdyna JK. Diluted magnetic semiconductors. J Appl Phys 1988;64:R29–64.
[2] Dalpian GM, Wei S-H, Gong XG, et al. Phenomenological band structure model of magnetic coupling in semiconductors. Solid State Commun 2006;138:353–8.
[3] Pan F, Song C, Liu XJ, et al. Ferromagnetism and possible application in spintronics of transition-metal-doped ZnO films. Mater Sci Eng R-Rep 2008;62:1–35.
[4] Sato K, Bergqvist L, Kudrnovský J, et al. First-principles theory of dilute magnetic semiconductors. Rev Mod Phys 2010;82:1633–90.
[5] Dietl T. A ten-year perspective on dilute magnetic semiconductors and oxides. Nat Mater 2010;9:965.
[6] Tu NT, Hai PN, Anh LD, et al. High-temperature ferromagnetism in heavily Fe-doped ferromagnetic semiconductor (Ga, Fe)Sb. Appl Phys Lett 2016;108:192401.
[7] Yang H-C, Gong B-C, Liu K, et al. The melilite-type compound $(Sr_{1-x}, A_x)_2MnGe_2S_6O$ (A = K, La) being a room temperature ferromagnetic semiconductor. Sci Bull 2018;63:887–91.
[8] Cervenka J, Katsnelson MI, Flipse CFJ. Room-temperature ferromagnetism in graphite driven by two-dimensional networks of point defects. Nat Phys 2009;5:840–4.
[9] Yazyev OV, Helm L. Defect-induced magnetism in graphene. Phys Rev B 2007;75:125408.
[10] Hod O, Barone V, Peralta JE, et al. Enhanced half-metallicity in edge-oxidized zigzag graphene nanoribbons. Nano Lett 2007;7:2295–9.
[11] Jung J, Pereg-Barnea T, MacDonald AH. Theory of interedge superexchange in zigzag edge magnetism. Phy Rev Lett 2009;102:227205.
[12] Wei S-H, Dalpian GM. Band coupling model of electron and hole mediated ferromagnetism in semiconductors: the case of GaN. Proceedings of the integrated optoelectronic devices 2008, 2008. SPIE.
[13] Bouzerar R, Bouzerar G, Ziman T. Non-perturbative V-J_{pd} model and ferromagnetism in dilute magnets. Europhys Lett 2007;78:67003.
[14] Chen L, Yang X, Yang F, et al. Enhancing the curie temperature of ferromagnetic semiconductor (Ga, Mn)As to 200 K via nanostructure engineering. Nano Lett 2011;11:2584–9.
[15] Žutić I, Zhou T. Tailoring magnetism in semiconductors. Sci China Phys Mech Astron 2018;61:067031.
[16] Anh LD, Hai PN, Tanaka M. Observation of spontaneous spin-splitting in the band structure of an n-type zinc-blende ferromagnetic semiconductor. Nat Commun 2016;7:13810.
[17] Li W, Kong L, Chen C, et al. Experimental realization of honeycomb borophene. Sci Bull 2018;63:282–6.
[18] Radisavljevic B, Radenovic A, Brivio J, et al. Single-layer MoS_2 transistors. Nat Nanotechnol 2011;6:147–50.
[19] Mak KF, Lee C, Hone J, et al. Atomically thin MoS_2: a new direct-gap semiconductor. Phy Rev Lett 2010;105:136805.

[20] Mak KF, McGill KL, Park J, et al. The valley hall effect in MoS_2 transistors. Science 2014;344:1489.
[21] Liu H, Neal AT, Zhu Z, et al. Phosphorene: an unexplored 2d semiconductor with a high hole mobility. ACS Nano 2014;8:4033–41.
[22] Li L, Yu Y, Ye GJ, et al. Black phosphorus field-effect transistors. Nat Nanotechnol 2014;9:372–7.
[23] Qiao J, Kong X, Hu ZX, et al. High-mobility transport anisotropy and linear dichroism in few-layer black phosphorus. Nat Commun 2014;5:4475.
[24] Yuan J, Chen W, Lou J. Two-dimensional heterostructure: perfect platform for exploring interface interaction. Sci Bull 2017;62:381–2.
[25] Cui Y, Li B, Li J, et al. Chemical vapor deposition growth of two-dimensional heterojunctions. Sci China Phys Mech Astron 2017;61:016801.
[26] Huang L, Zhong M, Deng H, et al. The coulomb interaction in van der Waals heterostructures. Sci China Phys Mech Astron, 62: 37311
[27] McGuire MA, Dixit H, Cooper VR, et al. Coupling of crystal structure and magnetism in the layered, ferromagnetic insulator CrI_3. Chem Mater 2015;27:612–20.
[28] Huang B, Clark G, Navarro-Moratalla E, et al. Layer-dependent ferromagnetism in a van der Waals crystal down to the monolayer limit. Nature 2017;546:270–3.
[29] Gong C, Li L, Li Z, et al. Discovery of intrinsic ferromagnetism in two-dimensional van der Waals crystals. Nature 2017;546:265–9.
[30] Wang Z, Zhang T, Ding M, et al. Electric-field control of magnetism in a few-layered van der Waals ferromagnetic semiconductor. Nat Nanotechnol 2018;13:554–9.
[31] Hao Z, Li H, Zhang S, et al. Atomic scale electronic structure of the ferromagnetic semiconductor $Cr_2Ge_2Te_6$. Sci Bull 2018;63:825–30.
[32] Bonilla M, Kolekar S, Ma Y, et al. Strong room-temperature ferromagnetism in VSe_2 monolayers on van der Waals substrates. Nat Nanotechnol 2018;13:289–93.
[33] Liu ZL, Wu X, Shao Y, et al. Epitaxially grown monolayer VSe_2: an air-stable magnetic two-dimensional material with low work function at edges. Sci Bull 2018;63:419–25.
[34] Tan C, Lee J, Jung S-G, et al. Hard magnetic properties in nanoflake van der waals Fe_3GeTe_2. Nat Commun 2018;9:1554.
[35] Deng Y, Yu Y, Song Y, et al. Gate-tunable room-temperature ferromagnetism in two-dimensional Fe_3GeTe_2. Nature 2018;563:94–9.
[36] Fei Z, Huang B, Malinowski P, et al. Two-dimensional itinerant ferromagnetism in atomically thin Fe_3GeTe_2. Nat Mater 2018;17:778–82.
[37] Wang C, Zhou X, Pan Y, et al. Layer and doping tunable ferromagnetic order in two-dimensional CrS_2 layers. Phys Rev B 2018;97:245409.
[38] Kan M, Adhikari S, Sun Q. Ferromagnetism in MnX_2 (X = S, Se) monolayers. Phys Chem Chem Phys 2014;16:4990–4.
[39] O'Hara DJ, Zhu T, Trout AH, et al. Room temperature intrinsic ferromagnetism in epitaxial manganese selenide films in the monolayer limit. Nano Lett 2018;18:3125–31.
[40] Zheng J, Cui Y, Li T, et al. Dielectric evidence for possible type-ii multiferroicity in α-$RuCl_3$. Sci China Phys Mech Astron 2018;61:057021.
[41] Miao N, Xu B, Zhu L, et al. 2*d* intrinsic ferromagnets from van der Waals antiferromagnets. J Am Chem Soc 2018;140:2417–20.
[42] Blöchl PE. Projector augmented-wave method. Phys Rev B 1994;50:17953–79.
[43] Kresse G, Joubert D. From ultrasoft pseudopotentials to the projector augmented-wave method. Phys Rev B 1999;59:1758–75.
[44] Kresse G, Furthmüller J. Efficient iterative schemes for ab initio total-energy calculations using a plane-wave basis set. Phys Rev B 1996;54:11169–86.
[45] Kresse G, Furthmüller J. Efficiency of ab-initio total energy calculations for metals and semiconductors using a plane-wave basis set. Comput Mater Sci 1996;6:15–50.
[46] Giannozzi P, Baroni S, Bonini N, et al. Quantum espresso: a modular and open-source software project for quantum simulations of materials. J Phys Condes Matter 2009;21:395502.
[47] Lee K, Murray ÉD, Kong L, et al. Higher-accuracy van der Waals density functional. Phys Rev B 2010;82:081101.
[48] Dion M, Rydberg H, Schröder E, et al. Van der Waals density functional for general geometries. Phy Rev Lett 2004;92:246401.
[49] Klimeš J, Bowler DR, Michaelides A. Van der Waals density functionals applied to solids. Phys Rev B 2011;83:195131.
[50] Hong J, Hu Z, Probert M, et al. Exploring atomic defects in molybdenum disulphide monolayers. Nat Commun 2015;6:6293.
[51] Qiao J, Pan Y, Yang F, et al. Few-layer tellurium: one-dimensional-like layered elementary semiconductor with striking physical properties. Sci Bull 2018;63:159–68.
[52] Hu Z-X, Kong X, Qiao J, et al. Interlayer electronic hybridization leads to exceptional thickness-dependent vibrational properties in few-layer black phosphorus. Nanoscale 2016;8:2740–50.
[53] Zhao Y, Qiao J, Yu P, et al. Extraordinarily strong interlayer interaction in 2*d* layered PtS_2. Adv Mater 2016;28:2399–407.
[54] Zhao Y, Qiao J, Yu Z, et al. High-electron-mobility and air-stable 2*d* layered $PtSe_2$ FETs. Adv Mater 2017;29:1604230.
[55] Perdew JP, Burke K, Ernzerhof M. Generalized gradient approximation made simple. Phys Rev Lett 1996;77:3865–8.
[56] Heyd J, Scuseria GE, Ernzerhof M. Hybrid functionals based on a screened coulomb potential. J Chem Phys 2003;118:8207.
[57] Heyd J, Scuseria GE, Ernzerhof M. Erratum: "Hybrid functionals based on a screened coulomb potential" [j. Chem. Phys. 118, 8207 (2003)]. J Chem Phys 2006, 124: 219906.
[58] Baroni S, de Gironcoli S, Dal Corso A, et al. Phonons and related crystal properties from density-functional perturbation theory. Rev Mod Phys 2001;73:515–62.
[59] Cococcioni M, de Gironcoli S. Linear response approach to the calculation of the effective interaction parameters in the lda+u method. Phys Rev B 2005;71:035105.
[60] Jiang P, Wang C, Chen D, et al. Stacking tunable interlayer magnetism in bilayer CrI_3 2018;arXiv:1806.09274.
[61] Xu C, Feng J, Xiang H, et al. Interplay between kitaev interaction and single ion anisotropy in ferromagnetic CrI_3 and $CrGeTe_3$ monolayers. npj Comput. Mater 2018;4:57.
[62] Kang P, Michaud-Rioux V, Kong XH, et al. Calculated carrier mobility of h-BN/γ-InSe/h-BN van der Waals heterostructures. 2D Mater 2017;4:045014.
[63] Kang P, Zhang W-T, Michaud-Rioux V, et al. Moiré impurities in twisted bilayer black phosphorus: effects on the carrier mobility. Phys Rev B 2017;96:195406.
[64] Gajdoš M, Hummer K, Kresse G, et al. Linear optical properties in the projector-augmented wave methodology. Phys Rev B 2006;73:045112.
[65] Nagaoka Y. Ferromagnetism in a narrow, almost half-filled *s* band. Phys Rev 1966;147:392–405.
[66] Qiu C, Liu F, Xu L, et al. Dirac-source field-effect transistors as energy-efficient, high-performance electronic switches. Science 2018;361:387.
[67] Sipe JE, Ghahramani E. Nonlinear optical response of semiconductors in the independent-particle approximation. Phys Rev B 1993;48:11705–22.
[68] Cao T, Wang G, Han W, et al. Valley-selective circular dichroism of monolayer molybdenum disulphide. Nat Commun 2012;3:887.
[69] Xiao D, Liu G-B, Feng W, et al. Coupled spin and valley physics in monolayers of MoS_2 and other group-VI dichalcogenides. Phy Rev Lett 2012;108:196802.
[70] Cong C, Shang J, Wu X, et al. Synthesis and optical properties of large-area single-crystalline 2d semiconductor WS_2 monolayer from chemical vapor deposition. Adv Opt Mater 2013;2:131–6.
[71] Aivazian G, Gong Z, Jones AM, et al. Magnetic control of valley pseudospin in monolayer WSe_2. Nat Phys 2015;11:148.
[72] Liu F, Zheng S, He X, et al. Highly sensitive detection of polarized light using anisotropic 2*d* ReS_2. Adv Funct Mater 2016;26:1169–77.
[73] Xia F, Wang H, Xiao D, et al. Two-dimensional material nanophotonics. Nat Photonics 2014;8:899.
[74] Tong W-Y, Gong S-J, Wan X, et al. Concepts of ferrovalley material and anomalous valley Hall effect. Nat Commun 2016;7:13612.
[75] Zhu Y, Kong X, Rhone TD, et al. Systematic search for two-dimensional ferromagnetic materials. Phys Rev Mater 2018;2:081001.
[76] Low T, Rodin AS, Carvalho A, et al. Tunable optical properties of multilayer black phosphorus thin films. Phys Rev B 2014;90:075434.
[77] Xia F, Wang H, Jia Y. Rediscovering black phosphorus as an anisotropic layered material for optoelectronics and electronics. Nat Commun 2014;5:4458.
[78] Beck J. Chalkogenidehalides of chromium. Synthesis, crystal structure, and magnetism of chromiumsulfidebromide, CrSBr. Z Anorg Allg Chem 1990;585:157–67.

Cong Wang is pursuing a doctor degree at Department of Physics, Renmin University of China. His research interest is electronic and magnetic properties of two-dimensional layered materials, manipulation of 2D materials through defects, strain or charge doping, and seeking novel 2-dimensional materials.

Wei Ji is a Professor of Physics at Department of Physics, Renmin University of China. He received his Ph.D. degree from the Institute of Physics, CAS in 2008. Prior to joining Renmin University of China, he spent four years at McGill University as a visiting scholar and then a postdoctoral fellow. As a computational physicist, his recent research focuses on surface and interface modeling of emerging low-dimensional electronic materials.